Extracting photon-number information from superconducting nanowire single-photon detectors traces via mean-derivative projection

I. S. Kuijf,[1,*] F. B. Baalbergen,[2,*] L. Seldenthuis,[2,*]
E. P. L. van Nieuwenburg,[1] and M. J. A. de Dood[2,†]
[1]*Lorentz Institute and Leiden Institute of Advanced Computer Science, Leiden University, P.O. Box 9506, 2300 RA Leiden, The Netherlands*
[2]*Huygens-Kamerlingh Onnes Laboratory, Leiden University, P.O. Box 9504, 2300 RA Leiden, The Netherlands*

(Received 17 November 2025; revised 17 March 2026; accepted 26 June 2026; published 28 July 2026)

Photon-number-resolved detection with superconducting nanowire single-photon detectors (SNSPDs) attracts increasing interest, often focusing on the rising edge of the electrical signal as the main source of photon-number-resolving information. It remains unclear whether additional photon-number information is contained in the rest of the detector response and how this can be optimally extracted and interpreted. In this work, we combine principal component analysis (PCA) with readout at relatively low sampling rates to explore the photon-number-resolving capabilities of SNSPDs. We find that the information of the photon number is captured by a single principal component that closely resembles the time derivative of the average response trace. Using the time derivative of the average response trace provides an agnostic method to obtain the photon number from SNSPD traces without the necessity of performing PCA, making this method simple and quick to calibrate. As an auxiliary diagnostic, we use a distinguishability metric based on the Bhattacharyya coefficient [Indian J. Statistics **7**, 401 (1946)] to quantify and compare the photon-number-resolving capabilities of different detector systems. Our analysis and interpretation of the principal components imply that photon-number resolution in SNSPDs can be achieved with moderate hardware requirements in terms of both sample rate (5 GS s^{-1}) and analog bandwidth (3 GHz) and could be implemented in a field-programmable gate array, giving a highly scalable solution for real-time photon counting.

DOI: 10.1103/dwth-wjtr

I. INTRODUCTION

Photon-number-resolving detectors are critical components for photonic quantum technologies. The ability to detect and distinguish between different numbers of photons with high fidelity underpins a wide range of quantum information protocols and is deemed essential for applications such as linear optical quantum computing [1,2], quantum metrology [3], and boson sampling [4]. Both high detection efficiency and accurate timing information are important for detecting quantum states of light with high fidelity and maintaining scalability in multiphoton experiments. Superconducting

*These authors contributed equally to this work.
†Contact author: dood@physics.leidenuniv.nl

Published by the American Physical Society under the terms of the Creative Commons Attribution 4.0 International license. Further distribution of this work must maintain attribution to the author(s) and the published article's title, journal citation, and DOI.

nanowire single-photon detectors (SNSPDs) act as single-photon threshold detectors that satisfy both requirements with system detection efficiencies exceeding 90% [5–7] combined with reset times of 10–50 ns [8–10] and timing jitter below 20 ps in commercially available systems [10–12].

Single-photon threshold detectors, such as single-photon avalanche photodiodes and conventional SNSPDs, traditionally only register the presence of at least one photon and do not count the number of photons. While this can be circumvented by using multiplexed detector arrays [13,14], an order of n^2 detectors are required to detect a state with n photons [15]. Recent work shows that SNSPDs themselves exhibit intrinsic photon-number-resolving capabilities [11,16–19], removing the need for multiplexing schemes. Cahall *et al.* [16] were the first to report photon-number dependence in SNSPDs, by measuring variations in the rise time of the SNSPD output signal that were attributed to differences in the initial hotspot resistance, which in turn depends on the photon number. This work was followed by several others exploring different strategies for extracting photon-number information from the analog signal, including linear fits to the slope of the rising edge [19], amplitude correlations [17], and measurements of the arrival time relative to a trigger signal [11].

Recently, Schapeler *et al.* [18] demonstrated that most of the photon-number-resolving information is concentrated within the rising edge of the electrical signal and can be extracted using a time-to-digital converter conditioned on a threshold. In their work, they compared measurements of the rising and falling edge arrival times with a principal component analysis (PCA) of the full electrical output signal of the detector. PCA is a technique widely used in multivariate statistics [20] that allows for identifying the most informative directions in the high-dimensional signal space, effectively reducing the complexity of the problem while preserving the photon-number-discriminating features.

Although this recent application of PCA successfully identifies the key discriminating regions of the signal trace, the origin and interpretation of the resulting principal components remains unclear. Treating PCA as a black-box statistical method limits its scalability, as it typically requires the offline collection of massive datasets and the postprocessing of singular value decompositions. Bridging this gap by understanding the physical contributions of the different principal components is essential for optimizing the photon-number-resolving capability of SNSPDs.

In this work, we address these questions by applying PCA to the electrical response traces of a commercially available SNSPD system. We show that the first principal component closely approximates the time derivative of the mean response trace, providing a direct physical explanation for how PCA isolates photon-number-dependent timing variations. Utilizing this insight, we introduce a mean-derivative projection technique that extracts photon-number information from the entire measured trace, as opposed to relying on isolated threshold points. This provides a method to obtain the photon number from SNSPD traces that is agnostic toward the measurement and optimization of experimental parameters. We show that this optimal projection can be done in an efficient and scalable way with modest hardware requirements, specifically a 5 GS s^{-1} sampling rate and a 3 GHz analog bandwidth, enabling real-time photon-number resolution (PNR). Finally, to characterize the photon-number resolvability obtained with this readout, we employ an easily calculated distinguishability metric based on the Bhattacharyya coefficient [21]. By directly quantifying the overlap of adjacent photon-number score distributions, this metric serves as a practical diagnostic tool to benchmark our PCA-derived mean-derivative projection against existing readout configurations.

II. DATA ACQUISITION

Detection events are collected using a commercial fiber-coupled SNSPD system (ID Quantique ID281), operated at 2 K in a closed-cycle refrigerator with cryogenic amplification at 40 K with unknown amplification and bandwidth. This detector is designed for a wavelength of 1550 nm and is biased at the manufacturer-recommended setting. A schematic overview of the measurement setup is shown in Fig. 1. To generate events, the detector is illuminated with attenuated laser pulses from a fiber-coupled laser diode (ID Quantique ID 3000) with a central wavelength of 1551 nm and a pulse

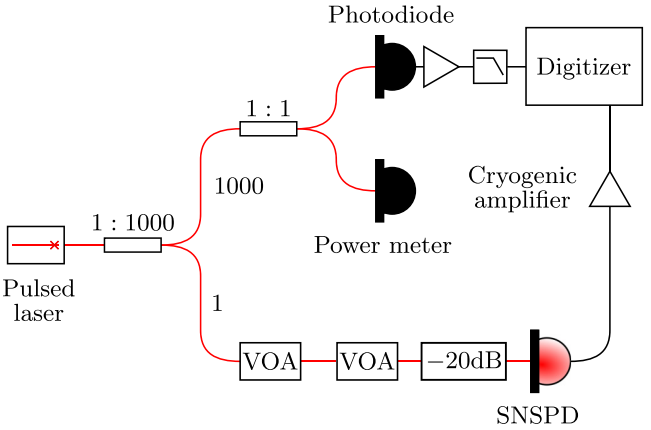


FIG. 1. Schematic overview of the experimental setup showing the laser, attenuators, and readout electronics.

length of 23 ps. The laser repetition rate is set to 500 kHz to ensure operation in a regime where the time between pulses is much larger than the thermal and electronic reset times of the SNSPD, thus not compromising the detection efficiency.

Light from the laser is coupled to a 1000:1 beam splitter, where the high-power output is divided equally between a fast photodiode for synchronization and a power meter (Thorlabs S122C) for monitoring the laser power. The low-power output is connected to two fiber-coupled variable optical attenuators (Thorlabs V1550F) and a fixed 20 dB attenuator (Thorlabs FA20T), before the light is coupled to the SNSPD. The variable optical attenuators are controlled using a voltage set by a computer, using the outputs of a digital-to-analog converter (National Instruments NI USB-6341). The transmission of the total system is carefully calibrated beforehand so that the set voltages on the variable optical attenuators and the measured power on the power meter are sufficient to calculate the mean photon number per pulse on the SNSPD.

The voltage signals from both the photodiode and SNSPD are sampled synchronously using two channels of a digitizer (Teledyne ADQ7DC) with an analog bandwidth of 3 GHz and a sample rate of 5 GS s^{-1}. The analog bandwidth is defined as the frequency where the signal is attenuated by 3 dB. Aliasing is not of concern due to the expected frequency response of SNSPDs consisting of mostly frequencies below 2 GHz [22,23]. The signal from the photodiode is used to trigger the digitizer and is filtered with a 190 MHz low-pass filter before being digitized. This stretches the pulse in the time domain and removes high-frequency noise from the signal to allow for a more precise determination of the arrival time of the laser pulse in postprocessing by fitting the peak position over more data points. The electronic SNSPD signal is attenuated with a 3 dB attenuator before sending it to the digitizer, to prevent signal clipping.

To form the dataset, 100 000 light traces of the SNSPD and the corresponding photodiode signals are recorded at 20 different mean photon numbers, resulting in a total of 2 000 000 measurements. The mean photon numbers range from $\mu = 0.003$ to $\mu = 2.55$ photons per laser pulse, and are logarithmically spaced to ensure a wide variety of input states within the dataset. The digitizer is triggered on the signal from the photodiode and records 512 samples per trace, including 20 samples before the trigger. In setting the attenuation, the external quantum efficiency is accounted for by measuring the efficiency of the complete system using quantum detector tomography [24], such that $\mu = \eta\langle n\rangle$ refers to the mean number of photons absorbed by the detector.

The digitizer triggering process introduces jitter due to its finite sample rate (5 GS s^{-1}), causing the trigger point to shift up to 200 ps compared to the true arrival time [25]. Because the jitter of the SNSPD system is much smaller than this offset [18,26,27], we correct for this digitizer-induced

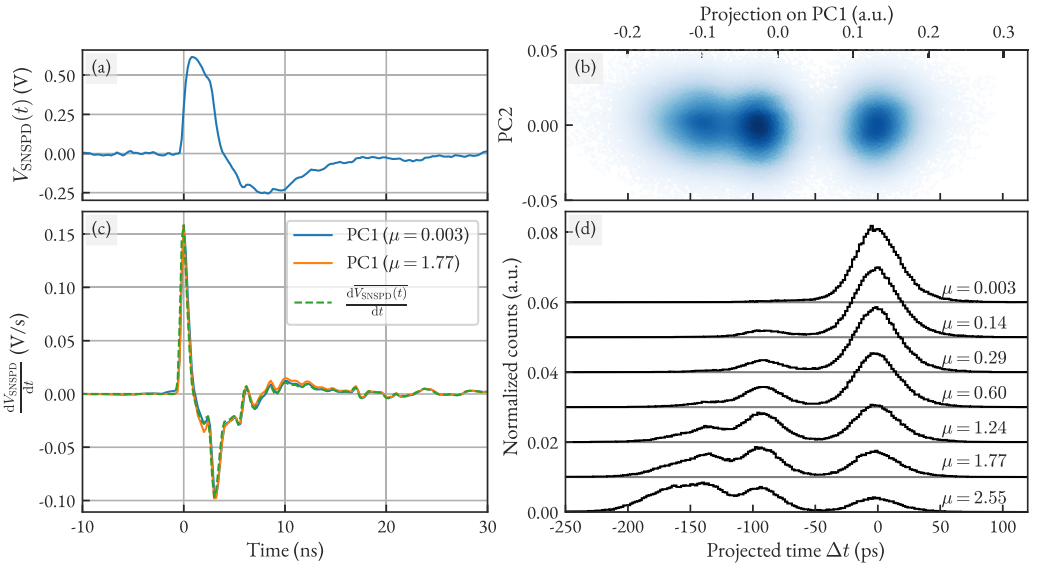


FIG. 2. Principal component analysis of detector pulses. (a) Time trace of the output signal of the SNSPD. (b) Example of the projection of the dataset at $\mu = 1.77$ to the first two principal components. (c) Comparison of the first principal component for $\mu = 0.003$ (blue), $\mu = 1.77$ (orange), and the average of the derivative of the output at $\mu = 0.003$ (green dashed line). (d) Projection of datasets of various mean photon numbers to the mean derivative of the $\mu = 0.003$ dataset. The results for projecting the data onto the first principal component of the $\mu = 0.003$ dataset are indistinguishable from the projection on the average derivative.

jitter by fitting a parabola to the top of the synchronization pulse to find the exact arrival time. This arrival time is then used to shift the SNSPD signal in postprocessing, by using the Fourier shifting theorem [28].

III. RESULTS

A. PCA: optimal photon-number resolution and interpretation

An example of a measurement trace is shown in Fig. 2(a). Fitting the PCA model yields 512 principal components, ranked according to the amount of variance in the dataset they capture. The time traces can be projected onto the principal components to reduce the dimensionality of the data. Figure 2(b) shows an example of this projection onto the first two principal components for traces with a mean absorbed photon number $\mu = 1.77$. We find that the first principal component contains most relevant photon-number information, which is apparent by the near-exclusive horizontal separation of clusters in Fig. 2(b) and this component's high explained variance (Appendix A).

The PCA is done separately for the different mean absorbed photon numbers μ, and we find consistent results across all datasets. The first principal components for the different datasets are all very similar to each other, as illustrated by the examples in Fig. 2(c). Also shown in the figure is the derivative of the mean trace of the dataset, which shows a remarkably strong resemblance to the first principal component. This suggests that photon-number information can be extracted by projecting the trace to the mean derivative of the dataset. To assign physical meaning to the values resulting from this projection, we approximate the detection traces for n photons, $V_n(t)$, as time-shifted variants of the one-photon trace, $V_1(t)$. This approximation is consistent with the observation that higher photon-number events produce steeper rising edges, which to first order can be approximated as a small time shift of an otherwise similar pulse shape. Under this assumption,

the projection can be written as

$$\mathrm{Proj}(V_n(t)) = \int_{\mathbb{R}} \frac{\mathrm{d}\overline{V_1(t)}}{\mathrm{d}t} V_n(t)\mathrm{d}t \approx \mathcal{C}\Delta t, \tag{1}$$

where $\mathcal{C}$ is a constant and Δt is a photon-number-dependent time shift. For more information on this approximation, see Appendix B. Equation (1) shows that the approximated time shift of the projected trace can be calculated as $\Delta t = \frac{1}{\mathcal{C}}\mathrm{Proj}(V_n(t))$. This projection to the mean derivative can thus be linked to a shift in time of the pulse under linear approximation and reproduces the PCA-based discrimination observed in the data. The results of the projection are shown in Fig. 2(d).

The mean derivative varies depending on the photon-number distribution and therefore changes slightly for the different mean photon numbers μ. As the mean derivative is a linear combination of the derivatives of the different photon numbers, the exact choice of which derivative to use for the projection only introduces an offset in the calculated time shift. In our analysis, we choose to use the mean derivative of the dataset corresponding to a mean photon number of $\mu = 0.003$. In this set, 99.85% of the light events are caused by the absorption of a single photon, making its mean trace highly similar to the mean trace of single-photon events, $\overline{V_1}$. Projection onto the derivative of the mean one-photon trace has the benefit that one-photon traces will be projected to the origin. Figure 2(d) shows the photon-number dependence for increasing mean photon numbers by the changing number and prominence of peaks, which agrees with the photon-number distribution of a coherent state as produced by a laser.

B. Photon-number resolvability

While existing metrics for PNR [29–31] provide valuable benchmarks, they often characterize different aspects of detector performance. To enable a direct comparison of the resolving power of our PCA-based readout with other extraction techniques, we use a simple, detector-centered metric. By defining a distinguishability metric based on the pairwise overlap of neighboring photon-number response distributions in the projected score space [30], we can quantify the pairwise overlap of neighboring photon-number responses without reference to a particular input-state distribution. This quantity serves as a simple diagnostic of nearest-neighbor resolvability and complements confidence-based or tomographic measures.

The pairwise distinguishability metric D is based on the Bhattacharyya coefficient [21], which gives values between 0 and 1 depending on the overlap between two underlying probability density functions. We define the probability density function of the projected time shift for an n-photon event as $G_{|n\rangle}(\Delta t)$. The distinguishability of resolving n photons then scales with the amount of overlap between the corresponding n-photon peak, $G_{|n\rangle}(\Delta t)$, and the consecutive peak, $G_{|n+1\rangle}(\Delta t)$. This consecutive peak $G_{|n+1\rangle}(\Delta t)$ is the limiting factor for the resolvability of n photons, as it has the highest overlap with $G_{|n\rangle}(\Delta t)$ [26]. This results in the following distinguishability metric:

$$D_{|n\rangle\to|n+1\rangle} = 1 - \int_{\mathbb{R}} \sqrt{G_{|n\rangle}(\Delta t) G_{|n+1\rangle}(\Delta t)}\mathrm{d}(\Delta t). \tag{2}$$

We note that D is not calculated directly from the histogram counts, but from the fitted probability density functions $G_{|n\rangle}$. Consequently, the accuracy of the resulting distinguishability values depends on how well the fitted distributions represent the measured histograms.

The histograms in Fig. 2(d) show peaks due to one-, two-, and more than three-photon events. In the present data, higher-order overlaps (e.g., between nonadjacent photon numbers) are negligible due to the well-separated nature of the peaks, such that the resolvability is effectively determined by nearest-neighbor terms (in particular, $D_{|1\rangle\to|2\rangle}$, while $D_{|1\rangle\to|3\rangle} \approx 0$). For detectors operating in a regime of low resolvability where non-neighboring overlaps become significant, a more complete metric would need to include these contributions. We identify three contributions in the histogram:

$$G_{\mathrm{total}}(\Delta t;\mu) = P_1(\mu)G_{|1\rangle}(\Delta t) + P_2(\mu)G_{|2\rangle}(\Delta t) + P_{3+}(\mu)G_{|3+\rangle}(\Delta t). \tag{3}$$

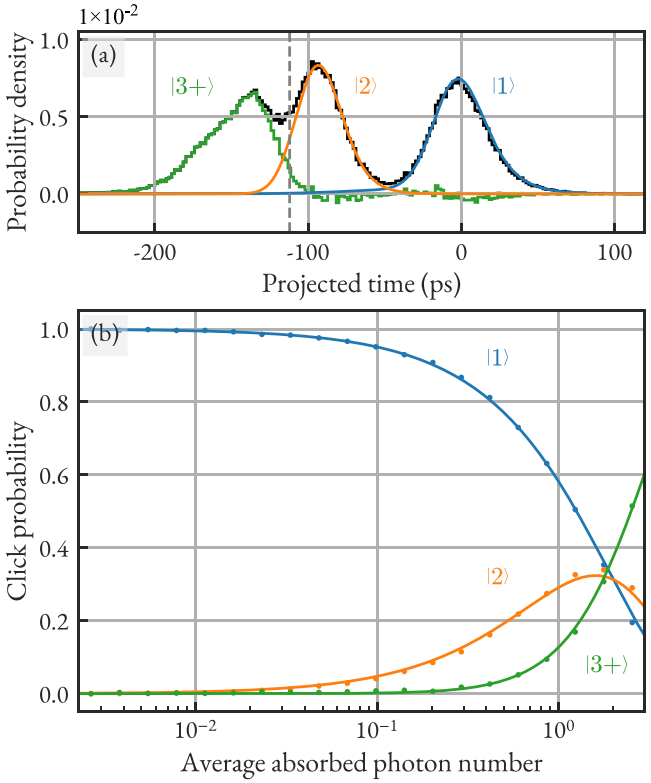


FIG. 3. Count statistics as a function of photon number. (a) Measured histogram (black) and fitted exponentially modified Gaussian distribution (blue and orange) for $\mu = 1.77$. The residuals are plotted in green. (b) Relative probability for the different photon numbers. The probabilities for one and two photons are directly derived from the Gaussian fit. The 3+ photon contribution is obtained by normalizing the residuals. The solid lines give the expected zero-truncated Poisson distribution.

Here, μ is the mean photon number of the distribution and $P_n(\mu)$ are the relative sizes of the different peaks in the histogram, the values of which are expected to follow the zero-truncated Poisson distribution. The probability density functions $G_{|n\rangle}(\Delta t)$ are well described by exponentially modified Gaussians (EMGs) [26,30,32], and are assumed to be independent of the mean photon number μ, which means that the shape of the EMG has to be fitted only once.

In order to find $G_{|1\rangle}(t)$, we fit the $\mu = 0.003$ data to a sum of an EMG and a Gaussian, to represent the one-photon peak and the small amount of residual counts not contained in the one-photon peak, respectively (see Fig. 7). For $\mu = 0.003$, almost all observed events (>99.8%) are caused by one-photon events. This fitted function $G_{|1\rangle}(\Delta t)$ is used to fit amplitude of the one-photon peak in the distributions for other values of μ. To fit the distributions for higher values of μ, P_1 is first fitted after which the one-photon peak is subtracted from the histogram and an EMG is fitted to the two-photon peak. The three-or-more photon contribution is obtained by calculating the residual of this fit, and is normalized and labeled by $G_{|3+\rangle}$. More complex decompositions of this residual are not uniquely constrained by the data, and we keep this contribution as a single aggregated residual. An example of the fit to the data at $\mu = 1.77$ is shown in Fig. 3(a). The fitted values of $P_n(\mu)$ are used to calculate the detection probabilities for n photons. These detection probabilities are compared to the expected zero-truncated Poisson distribution in Fig. 3(b), where a clear agreement can be seen.

Using the fitted probability density functions, we calculate the pairwise distinguishability of adjacent photon numbers from Eq. (2). We find the distinguishability to be $D_{|1\rangle\to|2\rangle} = 0.81 \pm 0.01$

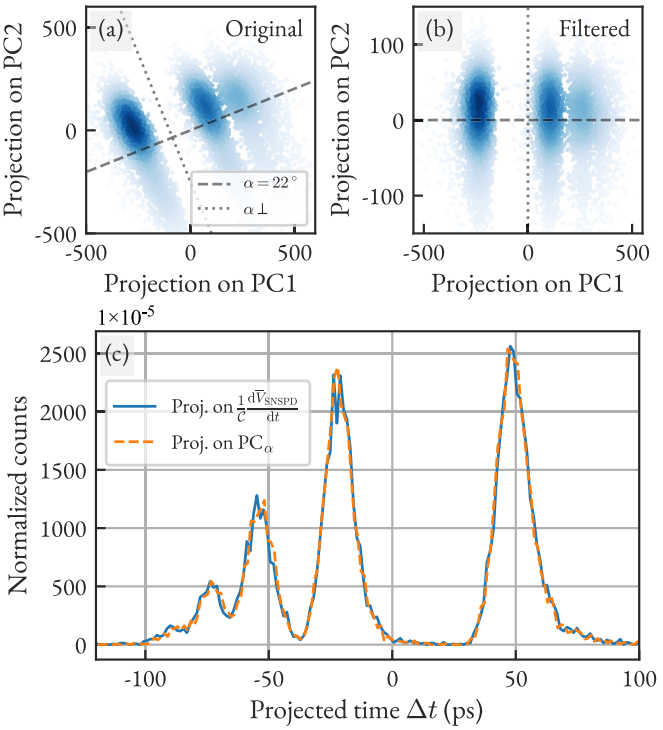


FIG. 4. Analysis of a subset of the dataset of Schapeler *et al.* [18] corresponding to a mean photon number of $\mu = 1.5$. (a) Projection on the first two principal components for the original data and (b) a filtered and down-sampled version of the dataset. The dashed and dotted lines indicate the projection and orthogonal axis used for assigning photon numbers to traces, respectively. (c) Histogram of the data projected onto the average derivative (blue) and onto the effective principal component PC$_\alpha$ (orange, dashed). The latter is linearly scaled and shifted to align with the derivative projection, allowing direct comparison.

and $D_{|2\rangle\to|3+\rangle} = 0.73 \pm 0.01$. The errors are found by random sampling from the fit parameters and calculating the variation in the distinguishability metric. This distinguishability metric does not depend on the mean photon number μ, as it is determined by using the fixed probability distributions.

IV. DISCUSSION

Previous methods to obtain photon-number information from time traces of SNSPDs used very high sample rates to digitize the electronic signal [18,33,34]. We show that using our technique it is possible to obtain similar results using a digitizer with a modest sample rate of 5 GS s^{-1}. This result is not limited to our dataset. We show this in Fig. 4 by applying our method to the open-source dataset of Schapeler *et al.* [35]. We use a subset of traces corresponding to a mean photon number of $\mu = 1.5$ and create a digitally down-sampled variant by applying a first-order bandpass filter with cutoffs at 10 MHz and 2 GHz, and then down-sampling from 128 to 4.92 GS s^{-1} by selecting every 26th sample point in each trace. We find that after filtering, all photon-number information shifts to the first principal component, ensuring that the clusters are now horizontally separated instead of diagonally, as can be seen in Figs. 4(a) and 4(b). This shift of information can be explained by investigating the vector in the direction of the clusters, PC$_\alpha$, and the vector perpendicular to that, PC$_{\alpha\perp}$ [Fig. 4(a)]. The perpendicular vector PC$_{\alpha\perp}$ shows a constant offset, meaning that this direction captures the variance in the overall dc offset of the data. By applying a first-order bandpass filter, this

TABLE I. Different PNR metrics for the data of Schapeler *et al.* at $\mu \approx 1.5$ and data obtained in this work at $\mu \approx 1.24$.

	Distinguishability D [Eq. (2)]		Confidence C_n [29]	
Transition	This work	Schapeler *et al.* [18]	This work	Schapeler *et al.* [18]
$\|1\rangle \rightarrow \|2\rangle$	0.83 ± 0.01	0.99 ± 0.01	0.959 ± 0.003	0.999 ± 0.002
$\|2\rangle \rightarrow \|3\rangle$	0.68 ± 0.01	0.99 ± 0.01	0.881 ± 0.003	0.996 ± 0.003
$\|3\rangle \rightarrow \|4\rangle$	–	0.85 ± 0.02	–	0.96 ± 0.01
$\|4\rangle \rightarrow \|5+\rangle$	–	0.7 ± 0.2	–	0.86 ± 0.07

dc offset gets removed from the data, collapsing all photon-number information to the first principal component.

To compare the photon-number-resolving capability of the filtered dataset with that of the original dataset, we plot the projection histograms in Fig. 4(c). The original, unaltered data are projected onto the effective principal component PC_α defined by Schapeler *et al.* [18], where the projection angle α is fitted for the specific subset of the data used here. The filtered data are projected onto the mean derivative of the filtered dataset. Figure 4(c) shows that the photon-number-resolving capability is equivalent for the original dataset and the digitally down-sampled variant, indicating that the significantly higher sample rate mainly enables better timing resolution in the signal trigger. Moreover, we find that the effective principal component needed for the projection to extract photon-number information is again closely approximated by the derivative of the mean trace.

An important distinction from similar methods is that our approach does not need to be tuned as it is largely agnostic to the detailed pulse structure and experimental parameters. Our method only requires measuring a small amount of response traces and taking the time derivative of the average trace. This means that recalibrating after changing an experimental parameter is quick and simple compared to other methods that would require refitting the PCA model on a large dataset.

The broad applicability of our method across different setups can be explained by approximating the photon-number dependence as a shift in time of an unclassified n-photon trace relative to the mean trace. The approximation of the photon-number dependence as a time shift is justified as higher photon-number events result in steeper rising edges, which in first order can be approximated as a time shift. This result is not specific to our detector, as Sidorova *et al.* [26,34] theoretically predict steeper rising edges for higher photon-number absorption events in long nanowires with multiple hotspots, suggesting that our method is applicable to any such detector.

To assess the photon-number-resolving capabilities of different detectors, we list the distinguishabilities D in Table I. The obtained distinguishabilities for the data of Schapeler *et al.* [18] are identical for both the PC_α projection of the original data and our mean-derivative projection of the filtered data, demonstrating that the mean-derivative projection retains the photon-number-resolving performance of the PCA-based projection. Comparing the two systems, our detector has a comparatively lower distinguishability $D_{1\rightarrow 2}$ compared to peaks with similar separation in the histogram from Schapeler *et al.* [18]. This difference can be attributed to a long tail in the one-photon peak in our detector, which increases the overlap between neighboring photon-number distributions (see Appendix C).

Other performance metrics have been proposed in previous works. Our proposed distinguishability metric D is comparable to the tomographic confidence metric introduced by Humphreys *et al.* [29] for continuous-output detectors. The two quantities characterize different aspects of detector performance. The metric proposed by Humphreys *et al.* calculates a Bayesian posterior probability, which mathematically requires assuming a prior distribution over the input states. In contrast, our distinguishability metric directly measures the overlap of the probability distributions $G_{|n\rangle}(\Delta t)$ and $G_{|n+1\rangle}(\Delta t)$ via the Bhattacharyya coefficient [21]. A different PNR benchmark was proposed by Schapeler *et al.* [30], which compares the separation of the arrival-time histograms to the width of these histograms and gives a single criterion for photon-number resolvability. By

comparison, our pairwise distinguishability metric provides a complementary state-by-state view of the nearest-neighbor photon-number resolvability.

The distinguishability depends on the width of the photon-number peaks in the projection histogram, which is directly related to the jitter in the system, constraining the resolving power. The mean full width at half maximum of the one-photon peak across all measured laser intensities for our system is $\Delta t_{|1\rangle} \approx (45 \pm 1)$ ps, as measured from the timing histograms from Fig. 2(d). The laser pulse length (23 ps) and the system jitter as measured by the manufacturer (35 ps) together contribute $\Delta t_{\text{system}} \approx (42 \pm 1)$ ps to the total measured jitter. We attribute the small difference to jitter introduced by the photodiode and the amplifiers connected to the photodiode. The SNSPD system is the main contributor to the total system jitter and thus the primary factor limiting the distinguishability. It is therefore expected that reducing the jitter in the SNSPD system will increase the PNR according to our metric.

SNSPDs with intrinsic timing jitter as low as 3 ps were demonstrated [36]. However, these low jitter values are obtained in short-nanowire detectors, where only a single hotspot can form [37]. For efficient detectors capable of PNR, longer meandering wires are needed and the jitter will mainly be determined by geometric jitter [27]. This means that there is an intrinsic trade-off between high detection efficiencies and the best PNR obtainable.

The mean-derivative projection method introduced to obtain optimum PNR can be implemented in a field-programmable gate array (FPGA). This can be performed by using a device similar to the digitizer used in this work. Our digitizer (Teledyne ADQ7) is capable of 300×10^6 pulse samples per second using pulse detection firmware. Using custom-made peak analysis, our device could be set up to perform our analysis to obtain the photon number [38,39]. Previous work on computationally similar calculations shows that even for relatively low speed FPGAs, the latency can be on the order of 10 µs [40]. This latency refers to processing delay and does not limit the rate at which events can be processed in a pipelined implementation. The first step of our original technique corrects for the digitizer-induced jitter by using a curve-fitting algorithm to find the trace-specific jitter, and corrects for this by Fourier shifting the trace. Although effective, this step is computationally expensive. We introduce an alternative method to correct for the digitizer-induced jitter and compute the projected time Δt in a way that requires minimal computations (details of this method are given in Appendix D). This technique paves the way for real-time photon-number classification when implemented in an FPGA and enables feedforward in quantum devices as a function of photon number [41–43].

V. CONCLUSIONS

We have demonstrated a systematic framework for identifying and interpreting photon-number resolution in SNSPDs using principal component analysis. Our results show that the first principal component corresponds to the derivative of the mean response trace, providing a physically intuitive and deterministic way to extract the photon-number information from digitized time traces. This method provides a direct and scalable route to photon-number determination that can be implemented with modest hardware requirements. To quantitatively evaluate the photon-number-resolving performance, we utilized a distinguishability metric based on the Bhattacharyya coefficient [21] of consecutive photon-number peaks. This analysis reveals that the distinguishability of our current setup is primarily limited by the SNSPD system jitter, guiding the potential for improvement of the photon-number-resolving capability. Finally, we demonstrated that our projection method generalizes across datasets and experimental setups, paving the way for real-time photon-number classification and feedforward operation in quantum photonic systems.

ACKNOWLEDGMENTS

The authors thank Mio Poortvliet and Wolfgang Löffler for use of the detector system. The authors thank Single Quantum B.V. for providing a preproduction engineering sample detector. This

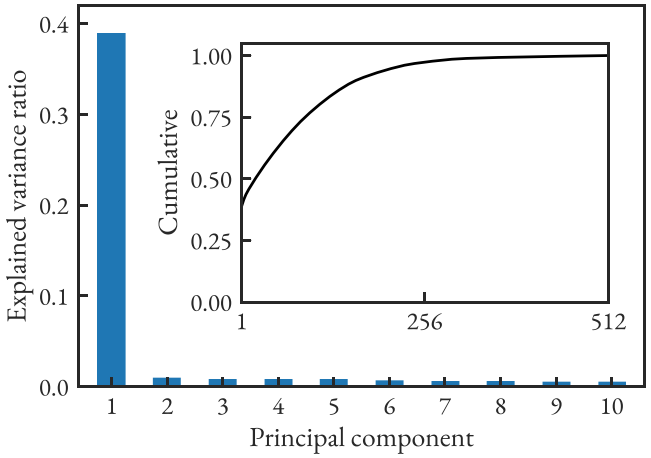


FIG. 5. Scree plot showing the explained variance of the first ten principal components in the principal component analysis for $\mu = 1.77$. The inset shows the cumulative explained variance as a function of the number of principal components.

research was made possible by financial support from the Dutch Research Council (NWO) under Project No. 19716. I.S.K. and E.P.L.v.N. acknowledge support from the Dutch National Growth Fund (NGF), as part of the Quantum Delta NL program.

DATA AVAILABILITY

There are no publicly available research data or software supporting this manuscript. Requests for further information or data should be sent to the authors.

APPENDIX A: SCREE PLOT OF PRINCIPAL COMPONENT ANALYSIS

Figure 5 shows the scree plot for our principal component analysis, where the principal components are naturally ordered by their explained variance. The first component accounts for most of the variance and is clearly more significant than the subsequent ones, indicating that most of the photon-number information is contained in PC1. This is corroborated by the inset, which shows the cumulative explained variance, indicating that about 200 principal components are needed to capture the remaining noise in the experimental data.

APPENDIX B: TIME-SHIFT APPROXIMATION

The classification of pulses to different photon numbers is done by projection of the detection trace to the mean derivative of all SNSPD traces. This projection can be linked to a time shift Δt if a linear approximation is used. For any differentiable function $f : \mathbb{R} \to \mathbb{R}$, the function can be approximated to first order in Δt as

$$f(t + \Delta t) \approx f(t) + \Delta t \frac{\mathrm{d}f(t)}{\mathrm{d}t}. \tag{B1}$$

Assuming that the detection trace for n photons can be approximated as a time-shifted version of the trace for one photon (see Fig. 6), we write

$$V_n(t) = V_1(t + \Delta t) \approx \overline{V_1(t)} + \Delta t \frac{\mathrm{d}\overline{V_1(t)}}{\mathrm{d}t}, \tag{B2}$$

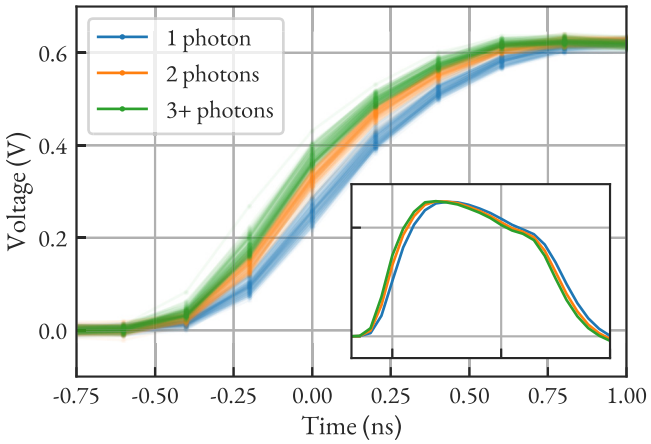


FIG. 6. Difference in rising edge of SNSPD traces. Measured traces, sampled at $5\,\mathrm{GS\,s^{-1}}$, are colored according to the classification as one photon (blue), two photons (orange), and three or more photons (green). The inset shows mean traces for a broader range, indicating that the time shift persists over a larger range.

where $V_n(t)$ is a detection trace for n photons and Δt is the time shift of V_n compared to V_1. Due to experimental noise, $V_1(t)$ is best estimated by averaging over all one-photon traces, denoted by $\overline{V_1(t)}$. Projecting $V_n(t)$ onto $\frac{\mathrm{d}\overline{V_1(t)}}{\mathrm{d}t}$, we find

$$\mathrm{Proj}(V_n(t)) = \int_{\mathbb{R}} \frac{\mathrm{d}\overline{V_1(t)}}{\mathrm{d}t} V_n(t)\mathrm{d}t \approx \int_{\mathbb{R}} \frac{\mathrm{d}\overline{V_1(t)}}{\mathrm{d}t}\left(\overline{V_1(t)} + \Delta t \frac{\mathrm{d}\overline{V_1(t)}}{\mathrm{d}t}\right)\mathrm{d}t. \tag{B3}$$

Since for all differential functions the function and its derivative are orthogonal, we can write the projection as

$$\mathrm{Proj}(V_n(t)) \approx \Delta t \int_{\mathbb{R}} \left(\frac{\mathrm{d}\overline{V_1(t)}}{\mathrm{d}t}\right)^2 \mathrm{d}t = \mathcal{C}\Delta t, \tag{B4}$$

where $\mathcal{C}$ is a normalization constant.

It is important to note that this first-order approximation implies that projection to the time derivative is equivalent to measuring a difference in arrival time, if the shape of the traces is similar enough. Here, we use $\overline{V_1}$ as a reference trace, but under the assumption that the different photon-number traces can be approximated as time-shifted versions of each other, this reference could also be the mean trace of the entire dataset.

APPENDIX C: TIMING HISTOGRAM FOR THE ONE-PHOTON PEAK

The one-photon peak of our detector consists of a main peak described by an EMG and a broad shoulder at the negative projected time. For an average absorbed photon number of $\mu = 0.003$, more than 99.8% of detected events should be one-photon events. In order to make a good estimate of the true one-photon response, we also fitted the shoulder of the count histogram. The physical origin of this shoulder is unclear, although similar secondary features were previously attributed to bends and/or imperfections in the meandering wire geometry [17,44]. Figure 7 shows the timing histogram for this photon number in a semilog scale with both the best EMG function (orange) and our best found function $G_{|1\rangle}(t)$ (blue). A clear improvement in the description of the one-photon peak can be seen for the EMG + Gaussian fit compared to the best-fitted EMG.

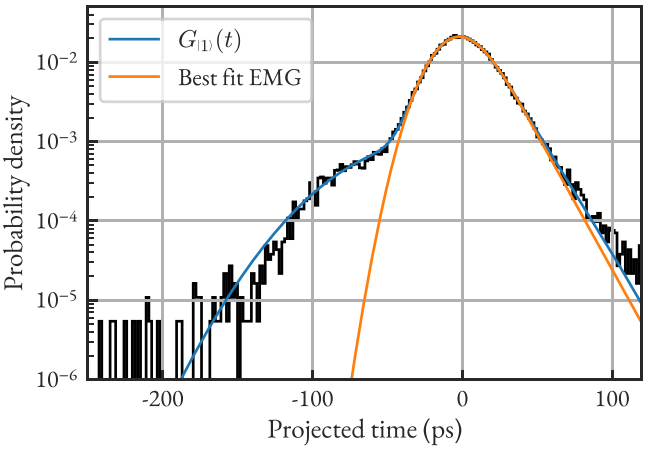


FIG. 7. Projected-time histogram for an average photon number of $\mu = 0.003$. The blue line shows the fitted function $G_{|1\rangle}(t)$ consisting of an EMG and an extra Gaussian. The orange line shows the best-fitted EMG function. The combined fit clearly shows better agreement with the measured data capturing also the shoulder near -100 ps.

APPENDIX D: HYBRID METHOD FOR SNSPD TRACE PROJECTION AND DIGITIZER JITTER CORRECTION

To decrease the computational load of our trace projection method and allow efficient implementation in an FPGA, we introduce an alternative method to correct for digitizer-induced jitter that uses unprocessed, non-time-shifted traces. We start by determining the trace-specific digitizer-induced jitter using the time-shift approximation introduced in Appendix B by calculating the time shift of each measured synchronization signal with respect to the mean synchronization signal. Then, after calculating the time shift of each measured SNSPD signal with respect to the mean one-photon trace, we subtract the corresponding time shift of the synchronization signal to recover the projected time. Mathematically, we project a measured pair of SNSPD and synchronization signal,

$$\vec{v}_{\text{measurement}} = (\vec{V}_{\text{SNSPD}}, \vec{V}_{\text{PD}})^T, \tag{D1}$$

onto

$$\vec{v}_{\text{projection}} = \left(\frac{1}{\mathcal{C}_{|1\rangle}} \partial \overline{V_{|1\rangle}}, -\frac{1}{\mathcal{C}_{\text{PD}}} \partial \overline{V_{\text{PD}}} \right)^T, \tag{D2}$$

to find the projected time

$$\Delta t = \vec{v}_{\text{measurement}} \cdot \vec{v}_{\text{projection}}. \tag{D3}$$

Here, $\partial \overline{V_{|1\rangle}} (\partial \overline{V_{\text{PD}}})$ is the mean derivative of the SNSPD (photodiode) and $\mathcal{C}_{|1\rangle} (\mathcal{C}_{\text{PD}})$ is a normalization constant calculated in Appendix B for the SNSPD (photodiode) trace. The projection vector is a constant for each measurement system and can be calculated before running the SNSPD.

APPENDIX E: COMPARISON BETWEEN PCA AND AVERAGE DERIVATIVE METHOD FOR A RESEARCH DETECTOR

To show the wide applicability of our method, we measured time traces from a fiber-coupled early-stage developmental prototype detector from Single Quantum with an approximate 60% external and 100% internal quantum efficiency [45]. This detector is mounted in a closed-cycle cryostat at 4.3 K and connected to a cryogenic amplifier (CMT-BA1) at 59 K via a 5 dB attenuator

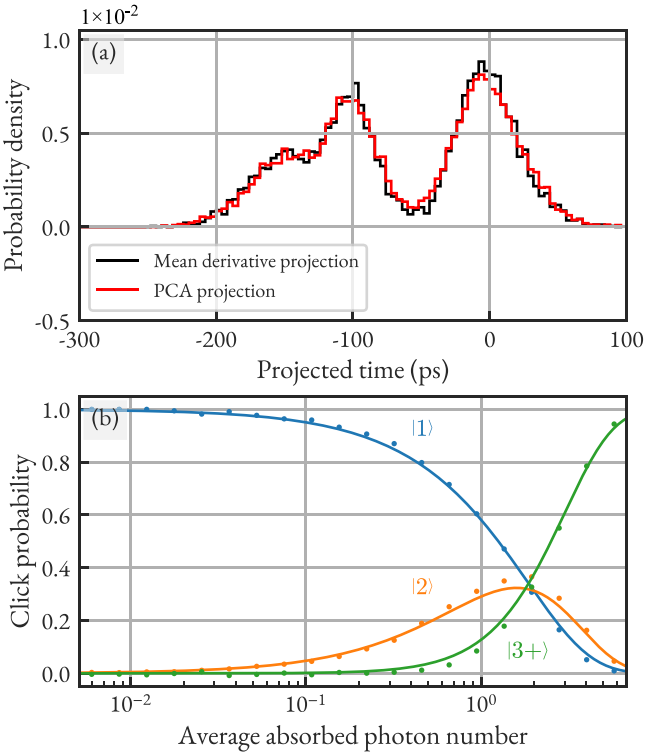


FIG. 8. Comparison of count statistics as determined by PCA and mean-derivative projection for the Single Quantum detector. (a) Measured mean-derivative projection histogram (black) and PCA projection histogram (red) for $\mu = 1.36$. (b) Relative click probability for the different photon numbers. The probabilities for one and two photons are directly derived from EMG fits. The solid lines give the expected zero-truncated Poisson distribution.

(minicircuits BW-S5W2+). The signal from the cryogenic amplifier is further amplified using a room temperature amplifier (Minicircuits ZFL-1000LN+) and sampled using the same method as described in the main text. This complete system contains low-frequency noise causing the baseline of the detector output to vary for all pulses. Furthermore, the detector is biased at a relatively low current due to the high temperature of the system, limiting the signal-to-noise ratio of the detector output.

To be able to perform PCA, the dc component of each trace is removed. This is done by subtracting the mean value from the first 50 data points of the data trace. The photon-number information is distributed over the first two principal components. The optimal projection angle is fitted and the resulting projection histogram for $\mu = 1.36$ is shown in Fig. 8(a) (red). From the original raw traces, without doing any preprocessing, the average derivative is calculated and the projection on each trace is calculated. The mean-derivative projection for $\mu = 1.36$ is also plotted in Fig. 8(a) (black), allowing a direct comparison of the measured timing histograms. This figure shows that the mean-derivative projection method results in a histogram that is very similar to the histogram of the PCA projection. The mean-derivative projection method requires fewer processing steps to achieve this result and can be applied to pulse data without additional training and verification that is needed for the PCA projection. Even with a noisy dataset, optimal PNR is obtained using this method, as demonstrated by the click probabilities in Fig. 8(b). The click probabilities are obtained by fitting EMG curves to both the one- and two-photon peaks using the same method as in the main text.

[1] L. You, Superconducting nanowire single-photon detectors for quantum information, Nanophotonics **9**, 2673 (2020).
[2] F. Grünenfelder, A. Boaron, G. V. Resta, M. Perrenoud, D. Rusca, C. Barreiro, R. Houlmann, R. Sax, L. Stasi, S. El-Khoury, E. Hänggi, N. Bosshard, F. Bussières, and H. Zbinden, Fast single-photon detectors and real-time key distillation enable high secret-key-rate quantum key distribution systems, Nat. Photonics **17**, 422 (2023).
[3] A. M. Bhargav, R. K. Rakshit, S. Das, and M. Singh, Metrology perspective of single-photon detectors: Review on global calibration methods, Adv. Quantum Technol. **4**, 2100008 (2021).
[4] H.-S. Zhong, H. Wang, Y.-H. Deng, M.-C. Chen, L.-C. Peng, Y.-H. Luo, J. Qin, D. Wu, X. Ding, Y. Hu, *et al.*, Quantum computational advantage using photons, Science **370**, 1460 (2020).
[5] J. Chang, J. W. Los, J. O. Tenorio-Pearl, N. Noordzij, R. Gourgues, A. Guardiani, J. R. Zichi, S. F. Pereira, H. P. Urbach, V. Zwiller, S. N. Dorenbos, and I. E. Zadeh, Detecting telecom single photons with $99.5 - 2.07 + 0.5\%$ system detection efficiency and high time resolution, APL Photonics **6**, 036114 (2021).
[6] D. V. Reddy, R. R. Nerem, S. W. Nam, R. P. Mirin, and V. B. Verma, Superconducting nanowire single-photon detectors with 98% system detection efficiency at 1550 nm, Optica **7**, 1649 (2020).
[7] P. Hu, H. Li, L. You, H. Wang, Y. Xiao, J. Huang, X. Yang, W. Zhang, Z. Wang, and X. Xie, Detecting single infrared photons toward optimal system detection efficiency, Opt. Express **28**, 36884 (2020).
[8] A. J. Kerman, D. Rosenberg, R. J. Molnar, and E. A. Dauler, Readout of superconducting nanowire single-photon detectors at high count rates, J. Appl. Phys. **113**, 144511 (2013).
[9] I. E. Zadeh, J. W. N. Los, R. B. M. Gourgues, V. Steinmetz, G. Bulgarini, S. M. Dobrovolskiy, V. Zwiller, and S. N. Dorenbos, Single-photon detectors combining high efficiency, high detection rates, and ultra-high timing resolution, APL Photonics **2**, 111301 (2017).
[10] I. E. Zadeh, J. W. N. Los, R. B. M. Gourgues, J. Chang, A. W. Elshaari, J. R. Zichi, Y. J. van Staaden, J. P. E. Swens, N. Kalhor, A. Guardiani, *et al.*, Efficient single-photon detection with 7.7 ps time resolution for photon-correlation measurements, ACS Photonics **7**, 1780 (2020).
[11] J. W. N. Los, M. Sidorova, B. Lopez-Rodriguez, P. Qualm, J. Chang, S. Steinhauer, V. Zwiller, and I. E. Zadeh, High-performance photon number resolving detectors for 850–950 nm wavelength range, APL Photonics **9**, 066101 (2024).
[12] J. Chang, I. E. Zadeh, J. W. N. Los, J. Zichi, A. Fognini, M. Gevers, S. Dorenbos, S. F. Pereira, P. Urbach, and V. Zwiller, Multimode-fiber-coupled superconducting nanowire single-photon detectors with high detection efficiency and time resolution, Appl. Opt. **58**, 9803 (2019).
[13] L. Stasi, G. Gras, R. Berrazouane, M. Perrenoud, H. Zbinden, and F. Bussières, Fast high-efficiency photon-number-resolving parallel superconducting nanowire single-photon detector, Phys. Rev. Appl. **19**, 064041 (2023).
[14] L. Stasi, T. Taher, G. V. Resta, H. Zbinden, R. Thew, and F. Bussières, Enhanced detection rate and high photon-number efficiencies with a scalable parallel SNSPD, ACS Photonics **12**, 320 (2025).
[15] M. Jönsson and G. Björk, Evaluating the performance of photon-number-resolving detectors, Phys. Rev. A **99**, 043822 (2019).
[16] C. Cahall, K. L. Nicolich, N. T. Islam, G. P. Lafyatis, A. J. Miller, D. J. Gauthier, and J. Kim, Multi-photon detection using a conventional superconducting nanowire single-photon detector, Optica **4**, 1534 (2017).
[17] D. Zhu, M. Colangelo, C. Chen, B. A. Korzh, F. N. C. Wong, M. D. Shaw, and K. K. Berggren, Resolving photon numbers using a superconducting nanowire with impedance-matching taper, Nano Lett. **20**, 3858 (2020).
[18] T. Schapeler, N. Lamberty, T. Hummel, F. Schlue, M. Stefszky, B. Brecht, C. Silberhorn, and T. J. Bartley, Electrical trace analysis of superconducting nanowire photon-number-resolving detectors, Phys. Rev. Appl. **22**, 014024 (2024).
[19] S. Sempere-Llagostera, G. S. Thekkadath, R. B. Patel, W. S. Kolthammer, and I. A. Walmsley, Reducing $g^{(2)}(0)$ of a parametric down-conversion source via photon-number resolution with superconducting nanowire detectors, Opt. Express **30**, 3138 (2022).
[20] H. Abdi and L. J. Williams, Principal component analysis, WIREs Comput. Stat. **2**, 433 (2010).

[21] A. Bhattacharyya, On a measure of divergence between two multinomial populations, Indian J. Statistics **7**, 401 (1946).

[22] A. J. Kerman, E. A. Dauler, W. E. Keicher, J. K. W. Yang, K. K. Berggren, G. Gol'tsman, and B. Voronov, Kinetic-inductance-limited reset time of superconducting nanowire photon counters, Appl. Phys. Lett. **88**, 111116 (2006).

[23] D. Zhu, M. Colangelo, B. A. Korzh, Q.-Y. Zhao, S. Frasca, A. E. Dane, A. E. Velasco, A. D. Beyer, J. P. Allmaras, E. Ramirez, W. J. Strickland, D. F. Santavicca, M. D. Shaw, and K. K. Berggren, Superconducting nanowire single-photon detector with integrated impedance-matching taper, Appl. Phys. Lett. **114**, 042601 (2019).

[24] F. B. Baalbergen, I. E. Zadeh, M. P. van Exter, and M. J. A. de Dood, Markov chain Monte Carlo detector tomography applied to a NbTiN nanobridge, Appl. Phys. Lett. **126**, 244007 (2025).

[25] *Manual ADQ7DC*, Teledyne SP Devices, 2019, https://www.spdevices.com/en-us/Products_/Documents/ADQ7DC/16-1796-E%20ADQ7DC%20manual.pdf.

[26] M. Sidorova, T. Schapeler, A. D. Semenov, F. Schlue, M. Stefszky, B. Brecht, C. Silberhorn, and T. J. Bartley, Jitter in photon-number-resolved detection by superconducting nanowires, APL Photonics **10**, 086113 (2025).

[27] N. Calandri, Q.-Y. Zhao, D. Zhu, A. Dane, and K. K. Berggren, Superconducting nanowire detector jitter limited by detector geometry, Appl. Phys. Lett. **109**, 152601 (2016).

[28] E. W. Weisstein, Fourier transform, https://mathworld.wolfram.com/FourierTransform.html (accessed 28 August 2025).

[29] P. C. Humphreys, B. J. Metcalf, T. Gerrits, T. Hiemstra, A. E. Lita, J. Nunn, S. W. Nam, A. Datta, W. S. Kolthammer, and I. A. Walmsley, Tomography of photon-number resolving continuous-output detectors, New J. Phys. **17**, 103044 (2015).

[30] T. Schapeler, I. Mischke, F. Schlue, M. Stefszky, B. Brecht, C. Silberhorn, and T. J. Bartley, Practical considerations for assignment of photon numbers with SNSPDs, APL Quantum **3**, 016102 (2026).

[31] J. Provazník, L. Lachman, R. Filip, and P. Marek, Benchmarking photon number resolving detectors, Opt. Express **28**, 14839 (2020).

[32] M. Sidorova, A. Semenov, H. W. Hübers, I. Charaev, A. Kuzmin, S. Doerner, and M. Siegel, Physical mechanisms of timing jitter in photon detection by current-carrying superconducting nanowires, Phys. Rev. B **96**, 184504 (2017).

[33] M. Endo, T. Sonoyama, M. Matsuyama, F. Okamoto, S. Miki, M. Yabuno, F. China, H. Terai, and A. Furusawa, Quantum detector tomography of a superconducting nanostrip photon-number-resolving detector, Opt. Express **29**, 11728 (2021).

[34] K. L. Nicolich, C. Cahall, N. T. Islam, G. P. Lafyatis, J. Kim, A. J. Miller, and D. J. Gauthier, Universal model for the turn-on dynamics of superconducting nanowire single-photon detectors, Phys. Rev. Appl. **12**, 034020 (2019).

[35] T. Schapeler, N. Lamberty, T. Hummel, F. Schlue, M. Stefszky, B. Brecht, C. Silberhorn, and T. J. Bartley, SNSPD traces given varying incident mean photon numbers, Zenodo, 2024, https://doi.org/10.5281/zenodo.10600595

[36] B. Korzh, Q.-Y. Zhao, J. P. Allmaras, S. Frasca, T. M. Autry, E. A. Bersin, A. D. Beyer, R. M. Briggs, B. Bumble, M. Colangel, *et al.*, Demonstration of sub-3 ps temporal resolution with a superconducting nanowire single-photon detector, Nat. Photonics **14**, 250 (2020).

[37] J. Yang, A. Kerman, E. Dauler, V. Anant, K. Rosfjord, and K. Berggren, Modeling the electrical and thermal response of superconducting nanowire single-photon detectors, IEEE Trans. Appl. Supercond. **17**, 581 (2007).

[38] *ADQ7DC–FWPD Datasheet*, Teledyne SP Devices, 2019, https://www.spdevices.com/en-us/Products_/Documents/FWPD/16-1793-ADQ7-FWPD-datasheet.pdf.

[39] *The Art of Pulse Detection*, Teledyne SP Devices, 2018, https://www.spdevices.com/en-us/Products_/Documents/Shared/18-2118-A_appnote_pulse_detection.pdf.

[40] Y. Pang, S. Wang, Y. Peng, N. J. Fraser, and P. H. W. Leong, A low latency kernel recursive least squares processor using FPGA technology, in *Proceedings of the 2013 International Conference on Field-Programmable Technology (FPT), Kyoto, Japan* (IEEE, Piscataway, NJ, 2013), pp. 144–151.

[41] M. Véstias, R. P. Duarte, J. T. de Sousa, and H. Neto, Parallel dot-products for deep learning on FPGA, in *Proceeding of 2017 International Conference on Field-Programmable Logic and Applications (FPL), Ghent, Belgium* (IEEE, Piscataway, NJ, 2017), pp. 1–4.

[42] A. Roldao Lopes and G. A. Constantinides, A fused hybrid floating-point and fixed-point dot-product for FPGAs, *Reconfigurable Computing: Architectures, Tools and Applications* (Springer, Berlin, Heidelberg, 2010), pp. 157–168.

[43] S. Mittal, A survey of FPGA-based accelerators for convolutional neural networks, Neural Comput. Appl. **32**, 1109 (2020).

[44] D. Wang, Y. Xiao, Z. Wan, C. Ding, H. Xu, J. Huang, J. Xiong, L. You, and H. Li, Origins and correction of secondary peaks in timing jitter of high-speed superconducting nanowire single-photon detectors, Appl. Phys. Lett. **128**, 162601 (2026).

[45] The efficiency of the early-stage developmental prototype provided by Single Quantum has not been optimized for system detection efficiency at the experimental wavelength.